PAPER

Experimental validation of contact resonance AFM using long massive tips

To cite this article: Nadav Zimron-Politi and Ryan C Tung 2023 *Nanotechnology* **34** 365712

IOP Publishing Nanotechnology
Nanotechnology 34 (2023) 365712 (16pp) https://doi.org/10.1088/1361-6528/acda37

Experimental validation of contact resonance AFM using long massive tips

Nadav Zimron-Politi and Ryan C Tung

Department of Mechanical Engineering, University of Nevada, Reno. 1664 N. Virginia St., Reno, Nevada NV-89557-0312, United States of America

E-mail: rtung@unr.edu

Received 27 February 2023, revised 3 May 2023
Accepted for publication 31 May 2023
Published 23 June 2023

Abstract

In this work, we present an experimental validation of a new contact resonance atomic force microscopy model developed for sensors with long, massive tips. A derivation of a new technique and graphical method for the identification of the unknown system parameters is presented. The technique and contact resonance model are experimentally validated. The agreement between our contact resonance experimental measurements and values obtained from nanoindentation show a minimal error of 1.4%–4.5% and demonstrate the validity of the new contact resonance model and system parameter identification technique.

Keywords: atomic force microscopy, contact resonance, nanomechanics

(Some figures may appear in colour only in the online journal)

1. Introduction

Contact resonance (CR) atomic force microscopy (AFM) utilizes the freely vibrating and in-contact resonance frequencies of the microcantilever sensor coupled with a sample of interest, to measure mechanical properties of the sample [1, 2]. CR measurements are performed in the linear, net-repulsive regime of the sensor-sample interaction, which allows for accurate nanoscale measurements. Traditionally in CR, a narrow, rectangular, cantilevered microbeam is utilized to measure the experimental eigenfrequencies. Then, the Euler–Bernoulli (E–B) beam equations are used to describe the relationship between the experimental eigenfrequencies and the sample's stiffness, which is then related to mechanical properties by means of contact mechanics.

In recent years, scientists have used AFM sensors equipped with nano-needles [3–10] and quartz tuning fork sensors [11–16] to probe biological samples in their natural physiological liquid environment, while the sensor's body remains out of the liquid and is therefore not affected by hydrodynamic forces (Trolling Mode). The colloidal probe is another form of large, massive-tip sensor, widely used by the AFM community [17–24] to probe samples that might be damaged from an ultra-sharp tip. The ability to probe the nanomechanical properties of biological samples is essential for using the AFM in medical diagnostics and healthcare [25–27]. With CR-AFM's capability to measure accurate nanomechanical properties, and the AFM's capability to probe biological samples using non-traditional sensors, a suitable CR model is required for the analysis of CR measurements performed using sensors with long, massive tips.

Recently, Jaquez-Moreno *et al* [28] developed a new CR model which includes the effect from tip length, mass, and rotational inertia, along with the sample's normal and lateral stiffness, hereinafter referred to as the Long-Massive-Tip Model (LMTM). This new model allows CR to be performed using non-traditional sensor tips such as colloidal probes, nano-needles, and quartz tuning forks, which all include tips with significant geometry. Modeling these novel geometries with simple traditional CR models will lead to significant error. Jaquez-Moreno *et al* [28] also presented a scheme for the determination of the system parameters that relies on a combination of transverse and torsional free eigenfrequencies, along with measurements of the sensor's dimensions. Scientists are continuously developing advanced AFM sensors for accurate measurements in challenging environments, hence, improved CR models and techniques are required to accommodate advanced new sensors and environmental effects.

In this work, we perform an experimental validation of the new CR model proposed in [28] in order to estimate the

degree to which the model is accurate, and to identify possible limitations of the model. Since the proposed new model includes inertial effects from the added mass and rotational inertia, which affect both the in-contact and freely vibrating measurements, the experimental measurements cannot be related to the corresponding eigenvalues by using the well-known clamped-free beam eigenvalues, as performed in traditional CR. Therefore, we propose new techniques for the solution, analysis, and accurate estimation of the system parameters, i.e. the added mass, rotational inertia, and general sensor properties, by utilizing multiple freely vibrating transverse eigenmodes. We propose a solution scheme which includes a direct solution to the system of nonlinear equations, and a graphical technique to examine the solution domain and possible multiplicity of the solution. Two examples are presented from our experimental setup and a third example problem illustrates the necessity for a graphical technique due to the possible existence of solution multiplicity.

Following the new techniques for the determination of system parameters based on freely vibrating eigenmodes, in-contact spectra are used from two sensors having added mass and rotational inertia. Additionally, in-contact spectra from a traditional AFM sensor are also used. The CR spectra are analyzed using a simple CR model along with the LMTM, and a comparison to nanoindentation data is presented for all CR results from the 3 different sensors and models. We include a discussion on the lower and upper bounds of the analytical eigenfrequencies of the system, and present in-contact experimental measurements of the 1st eigenmode with a frequency higher than the freely vibrating 2nd eigenmode. To the best of our knowledge, this is the first time in-contact spectra are measured at a higher frequency than the immediately subsequent out-of-contact eigenmode. Such behavior contradicts with conventional CR models, that predict an upper bound for the in-contact eigenfrequency that is lower than the immediately subsequent eigenmode free frequency, nevertheless, such behavior is well-described by the LMTM.

2. Theory

In CR-AFM, the freely vibrating cantilever sensor eigenfrequencies (out of contact), along with the in contact ones, are measured experimentally. E–B beam models are used to describe the microsensor-sample vibrational system with different types of boundary conditions. The boundary conditions on one side of the beam are clamped, while the boundary conditions on the contact side are chosen to accommodate different effects. The most widely used CR model includes a single normal spring located near the beam end, hereinafter referred to as the Single Spring Model (SSM) [2]. Traditionally, the sensors used to perform CR are equipped with basic AFM tips, usually around 10–15 μm in length. If one wishes to include the effect of the tip length, then a lateral spring may also be included, which together create a moment about the point of tip connection with the beam. Researchers have also been able to measure the samples's visco-elastic properties by including a normal and lateral damper element in parallel with the aforementioned springs [29]. The effect of the tilt angle between the microsensor and the sample is also included in some references (for example [29, 30]). The effect from tilt angle can only be estimated with the AFM manufacturer's nominal design specifications, which does not take into consideration the inherent tilt of the sample which may change in every setup.

The post-processing of CR-AFM measurements requires the use of a characteristic equation formed from the solution of the E–B free vibration problem with the corresponding boundary conditions. The characteristic equation includes the system parameters and is written in terms of the countably infinite eigenvalues of the system $\beta_n L$, where n is the nth wave number of the system. The dispersion relation between the eigenvalues and the natural frequencies of the beam is given by [31]:

$$f_n = \frac{(\beta_n L)^2}{2\pi}\sqrt{\frac{EI}{\rho A L^4}}, \tag{1}$$

where E is the Young's modulus of the cantilever, I is the second area moment of inertia, ρ is the mass density, A is the cross-sectional dimension, and L is the beam length.

If the effects of the tip mass and rotational inertia are neglected, as in traditional CR, the experimentally measured eigenfrequencies can be converted to the eigenvalues using the dispersion relation given in equation (1). The characteristic equation of the system, in the case that the cantilever tip is out of contact ('free case'), reduces to the well-known form of a clamped-free cantilever beam: $\cos(\beta_n L)\cdot\cosh(\beta_n L)+1=0$. By taking the ratio of equation (1) for the in-contact and out-of-contact eigenfrequencies, and using the eigenvalues of the clamped-free vibrating cantilever, we are able to directly find the in-contact eigenvalues without prior knowledge of E, I, ρ, A and L. This ratio leads to:

$$\beta_n L = \beta_n^0 L\sqrt{\frac{f_n}{f_n^0}}, \tag{2}$$

where $\beta_n^0 L$ are the roots of the clamped-free cantilever beam equation, f_n is the in-contact experimental natural frequency, and f_n^0 is the out-of-contact corresponding experimental natural frequency. If the tip's mass and rotational inertia cannot be neglected, the out-of-contact eigenvalues are unknown and they are a function of the tip's added mass and rotational inertia. For such cases, we propose rewriting equation (1) in the following form: $f_n = (\beta_n L)^2/\tilde{C}$, thus we may define:

$$\beta_n L = \sqrt{f_n\cdot\tilde{C}}, \tag{3}$$

where $\tilde{C}=2\pi\sqrt{\frac{\rho AL^4}{EI}}$. Rabe *et al* [2] considered the effect of a mass located at the cantilever end on the vibration of the system, with the use of beam dimensions and mechanical properties, to calculate a system constant, similar to our defined $\tilde{C}$. Muraoka [32] modified a commercial sensor by

adding a tungsten particle to the beam end. Muraoka used the spectra before and after the attachment to estimate the missing data encapsulated in $\tilde{C}$. Recently, Jaquez-Moreno *et al* [28] also used the beam dimensions and mechanical properties in their numerical work, to relate the experimental eigenfrequencies to the corresponding eigenvalues. The approach taken by Muraoka cannot be performed when a commercial sensor is purchased with a large, massive tip and the spectra can only be measured with the massive tip. Calculating $\tilde{C}$, or any of the system parameters, based on its definition is prone to error as discrepancies between calculated and measured values were previously published [33, 34], likely due to deviation between the experimental results and the theoretical models. The approaches described in the referenced literature rely on *a priori* knowledge of the sensor's dimensions, or, of the un-tipped system, and for both cases such information might not be available or may be misleading.

A new technique is presented next for the solution, analysis, and estimation of the unknown system parameters, relying solely on the sensor's free transverse eigenfrequencies, as in traditional CR practice. This proposed technique can be used with any characteristic equation and dispersion relation and does not rely on any prior measurements of the un-tipped system (if one exists), or of the sensor's dimensions. The development of the new technique is presented here for the model presented in [28].

2.1. System parameters solution, analysis, and estimation technique

Considering the characteristic equation introduced by Jaquez-Moreno *et al* [28] while the cantilever is out of contact, the characteristic equation is a function of three parameters: the eigenvalue βL, the nondimensional tip mass $\Delta = \frac{m_t}{\rho A L}$, and the nondimensional rotational inertia $\hat{I}_t = \frac{I_t}{\rho A L^3}$ (m_t and I_t are the tip's mass and rotational inertia respectively):

$$\begin{aligned}&[(-2\Delta\hat{I}_t(\beta L)^8 + 2(\beta L)^4)\cos(\beta L) + 6(\beta L)\\ &\quad \sin(\beta L)(-\hat{I}_t(\beta L)^6/3 - \Delta(\beta L)^4/3)]\cosh(\beta L)\\ &\quad +6(\beta L)(-\hat{I}_t(\beta L)^6/3 + \Delta(\beta L)^4/3)\sinh(\beta L)\cos(\beta L)\\ &\quad +2\Delta\hat{I}_t(\beta L)^8 + 2(\beta L)^4 = 0.\end{aligned} \tag{4}$$

Inserting equation (3) into the characteristic equation given in equation (4), and using three experimental freely vibrating bending eigenfrequencies, we may solve the resulting system of nonlinear equations numerically for the three unknowns: $\tilde{C}$, Δ, and $\hat{I}_t$, hereinafter, denoted as the 3-Mode approach. Once $\tilde{C}$ is found, we may use it in equation (3) along with the experimental in-contact natural frequencies, to calculate the eigenvalues and continue with common CR post-processing methods. For the cases in which the characteristic equation does simplify to the clamped-free case, equation (3) will produce the same results as equation (2).

The solution to the system of 3 nonlinear equations described above may lead to several solutions. While searching for a physically meaningful solution, i.e. positive system parameters in proximity to nominal values, the use of a graphical or visual representation of the system may be beneficial for better understanding of the solution domain. The system of equations is formed from the characteristic equation, which is a transcendental equation in βL. The countably infinite zeros of the equation correspond to the infinite eigenvalues of the system. A 3D plot of the system is not practical for analysis as the surfaces created to represent the characteristic equation, spanned by values of Δ and $\hat{I}_t$, are discontinuous due to the nature of the hyperbolic functions forming the characteristic equation. A different approach, to address this issue, for graphical representation is presented in the next section.

2.2. Graphical representation by a minimization technique

In this section, by considering some of the algebraic equations introduced above, we formulate a set of new equations identically equal to zero. We evaluate the non-zero side of the new equations for a range of values assigned to our unknown system parameters, and seek a combination of system parameter values that minimizes the equality. These new equations are used as objective functions, as we seek to minimize, or 'zero', the error by properly selecting the system parameters. Equation (4) has a countably infinite number of eigenvalue solutions but can be solved to find a specific eigenvalue $\beta_n L$ for any given set of Δ and $\hat{I}_t$. Considering equation (3), we are able to perform algebraic manipulations that will allow us to create an objective function which is evaluated numerically for every set of Δ and $\hat{I}_t$. By evaluating the objective function over a physically realistic domain of Δ and $\hat{I}_t$, we may find the minimum of the objective function in the domain. The minimum value of the objective function corresponds to a specific set of Δ and $\hat{I}_t$ values which are the desired system parameters values. The objective function is formed from the first three eigenvalues of equation (4) and the first three experimental free eigenfrequencies. Taking the ratio of equation (3) for three sets of eigenvalues and experimental free eigenfrequencies leads to: $\frac{\beta_2 L}{\beta_1 L} - \sqrt{\frac{f_2^0}{f_1^0}} = 0$ and $\frac{\beta_3 L}{\beta_1 L} - \sqrt{\frac{f_3^0}{f_1^0}} = 0$. Adding the sets leads to our first objective function:

$$\frac{\beta_2 L - \beta_3 L}{\beta_1 L} - \frac{\sqrt{f_2^0} - \sqrt{f_3^0}}{\sqrt{f_1^0}} = 0. \tag{5}$$

Any numerical deviation of the left hand side of equation (5) from a value of zero is considered an error which we wish to minimize by selecting a proper set of Δ and $\hat{I}_t$. The above set of 3 eigenvalues and experimental frequencies may be written in 2 additional forms which will lead to different error values:

$$\frac{\beta_1 L - \beta_3 L}{\beta_2 L} - \frac{\sqrt{f_1^0} - \sqrt{f_3^0}}{\sqrt{f_2^0}} = 0, \tag{6}$$

$$\frac{\beta_1 L - \beta_2 L}{\beta_3 L} - \frac{\sqrt{f_1^0} - \sqrt{f_2^0}}{\sqrt{f_3^0}} = 0. \tag{7}$$

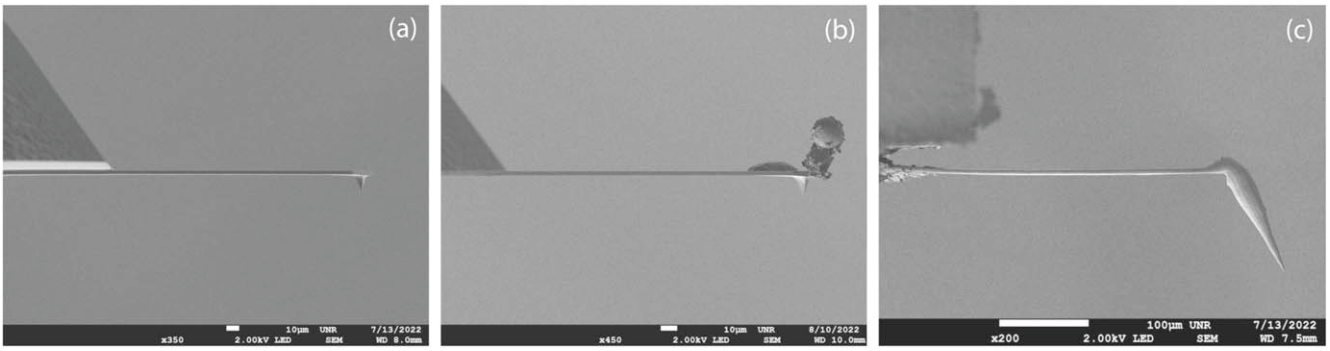

Figure 1. Sensors used in this work for CR spectra. Images taken using a Scanning Electron Microscope (SEM). (a) HQ-75-Au unmodified silicon sensor. (b) HQ-75-Au modified silicon sensor. (c) 25Pt300B large tip platinum sensor.

Table 1. Properties measured during AFM experimental setup and using SEM of the HQ-75-Au sensor unmodified (No bead attached) and modified (With bead attached) sensors.

Property	As measured	Remarks
L [μm]	210.8	Length of sensor
b [μm]	32.7	Width of sensor
h [μm]	3.0	Thickness of sensor
d_{bead} [μm]	14.7 and 19.2	Diameter of attached bead
$f^0_{1,\text{NB}}$ [kHz]	79.9	Freely vibrating transverse 1st eigenfrequency, No bead attached
$f^0_{2,\text{NB}}$ [kHz]	504.3	Freely vibrating transverse 2nd eigenfrequency, No bead attached
$f^0_{3,\text{NB}}$ [kHz]	1418.6	Freely vibrating transverse 3rd eigenfrequency, No bead attached
$f^0_{1,\text{WB}}$ [kHz]	50.2	Freely vibrating transverse 1st eigenfrequency, With bead attached
$f^0_{2,\text{WB}}$ [kHz]	420.1	Freely vibrating transverse 2nd eigenfrequency, With bead attached
$f^0_{3,\text{WB}}$ [kHz]	1239.3	Freely vibrating transverse 3rd eigenfrequency, With bead attached
$f^0_{4,\text{WB}}$ [kHz]	2409.3	Freely vibrating transverse 4th eigenfrequency, With bead attached

Furthermore, equation (3) can be manipulated algebraically in many ways to produce an infinite number of objective functions. Taking the 2nd power of equation (3) and manipulating similarly leads to:

$$\frac{(\beta_2 L)^2 - (\beta_3 L)^2}{(\beta_1 L)^2} - \frac{f_2^0 - f_3^0}{f_1^0} = 0. \tag{8}$$

Though this type of manipulation does not contain any additional information, it increases the error for erroneous values of Δ and $\hat{I}_t$, while the correct set of Δ and $\hat{I}_t$ is not affected by this type of manipulation. Since our system involves two system parameters, we choose to visualize the objective function error using a heatmap, for a range of Δ and $\hat{I}_t$ values. The large error values caused by taking equation (3) to some power helps magnify the minimum solution. Another set of algebraic manipulation can also lead to:

$$\frac{(\beta_1 L)^2}{f_1^0} + \frac{(\beta_2 L)^2}{f_2^0} - 2\frac{(\beta_3 L)^2}{f_3^0} = 0, \tag{9}$$

which once again can be written in 3 different forms Each objective function may produce a curve of minimum error with no unique zero value, unless the exact values of Δ and $\hat{I}_t$ are met. The minimum error curves, produced from several objective functions, all cross at a unique value of Δ and $\hat{I}_t$ which is a solution of the system and has a zero value of the objective functions. Similarly, we can choose to sum the absolute value of each objective function, which results in a summation of near zero values at the pixels near the solution, and very high error values in the remaining domain. This also leads to a new objective function which converges to a minimum point with best results.

The presented minimization technique allows the user not only to find the system parameters, but also to explore any domain of the system parameters, which might become vital for the proper distinction between multiple solutions that may occur. The example problems presented next, illustrate the use of the 3-Mode approach and the minimization technique for the estimation of the system parameters using free eigenfrequency data only, prior to performing CR. Furthermore, we present an additional example to illustrate the possibility of system parameter solution multiplicity.

Table 2. System parameters as calculated using different approaches for the modified sensor. *Also using densities of the silicon cantilever and borosilicate beads: $\rho_{Si} = 2330\ \mathrm{kg\ m^{-3}}$, and $\rho_{BS} = 2200\ \mathrm{kg\ m^{-3}}$.

Source of data	$\hat{I}_t$	Δ	$\tilde{C}$[sec]
Estimated based on SEM measurements *	0.0031	0.3000	3.8468×10^{-5}
Three transverse modes, no information before bead attachment (3-Mode approach)	8.7626×10^{-4}	0.5331	3.9247×10^{-5}
Three transverse modes before bead attachment	N/A	N/A	$f^0_{1,NB} \Rightarrow 4.4023 \times 10^{-5}$ $f^0_{2,NB} \Rightarrow 4.3696 \times 10^{-5}$ $f^0_{3,NB} \Rightarrow 4.3491 \times 10^{-5}$

2.3. Example problem 1: modified sensor

An AFM sensor of type HQ-75-Au (Oxford Instruments) is modified using an added micro borosilicate (BS) glass bead glued on the top side of the cantilever (opposite to tip side). The added bead allows us to examine the 3-Mode approach and the graphical heatmap representation discussed above, for determining the system parameters. Figure 1(a) shows the sensor before the modification and figure 1(b) shows a side view of the modified sensor showing the tip and 2 BS beads attached. The sensor's dimensions and free eigenfrequencies are given in table 1 before the attachment of the bead (subscript NB) and after (subscript WB).

Using $f^0_{1,\mathrm{WB}}$, $f^0_{2,\mathrm{WB}}$, and $f^0_{3,\mathrm{WB}}$ along with equation (3) we can solve equation (4) for $\hat{I}_t$, Δ, and $\tilde{C}$. Table 2 summarizes the system parameters obtained by the 3-Mode approach along with calculating the parameters based on their definition and calculating $\tilde{C}$ directly using equation (1) and the corresponding eigenvalues of the clamped-free characteristic equation before the attachment of the beads. The differences in the value of the system parameters are due to the variation between the base assumption of the theoretical model described in equation (4) from the actual setup, and the ability of the theoretical model to capture all real-life physics. Thus, the model uses a point mass and a point rotational inertia located at the distal end of the beam, to encapsulate the effect from a real world massive tip located near the beam end, leading to the discrepancies reported in table 2. The adhesive used to attach the beads is an additional mass component not included in the estimates and might also have some effect on the bending stiffness of the cantilever probe.

Once the system parameters are found, we may use equation (4) along with equation (3) to calculate any higher free eigenfrequency of the cantilever and compare to the experimental measurements. For this example, the difference from the calculated 4th eigenfrequency and the measured one is about ~1.7% which indicates that the suggested model [28] describes the experimental system well.

Along with the 3-Mode approach discussed above, we use the graphical minimization technique for the determination of Δ and $\hat{I}_t$. In the development of the Objective Functions (OF), we take the ratio of two dispersion relations, canceling out $\tilde{C}$ and reducing the dimensionality of the problem. The remaining system parameters Δ and $\hat{I}_t$ are nondimensional parameters. Once Δ and $\hat{I}_t$ are found based on the combination that lead to a minimum error, the corresponding nondimensional eigenvalues are related to the dimensional eigenfrequency using $\tilde{C}$ having dimensions of time. For a specific domain of interest for Δ and $\hat{I}_t$ shown in figure 2, we divide the domain into a discrete number of subdivisions and calculate the error based on the Δ and $\hat{I}_t$ at every point. The minimum error from each OF may grow rapidly just a few pixels away, and is also sensitive to the number of divisions used. In the error heatmaps presented in this manuscript, we use a high number of divisions which leads to a minimum error located at a point that is hard to distinguish. Since we are using the minimum curve and not a minimum point, we focus on the curve rather than the minimum value. The minimum curves obtained by the 3 different OFs used in this example are plotted on top of each other in figure 2(d), and their crossing leads to the same solution obtained using the 3-Mode approach. Any 2 minimum curves can be used to find the crossing solution, nonetheless, we use 3 different objective function minimum curves, that are very distinct from one another, to better highlight the solution procedure. By increasing the number of divisions per a fixed range of Δ and $\hat{I}_t$, we minimize the error by better estimating the system parameters. In this example, the Δ and $\hat{I}_t$ solution corresponding to the minimum error show a convergence to a unique solution, as seen in figure 3.

2.4. Example problem 2: sensor with large tip

In this example, we use the 3-Mode approach to calculate the system parameters of an AFM sensor of type 25Pt300B (Rocky Mountain Nanotechnology), hereinafter referred to as RMN sensor. The RMN sensor is a unique solid platinum (Pt) probe, normally used for electrical measurements, which includes a very large cone shape tip, with a size comparable to the length of the cantilever beam. A side view of the RMN sensor is given in figure 1(c) and general dimensions and free frequencies are given in table 3.

Once again, after the system parameters are determined, we use equation (4) along with equation (3) to calculate the 4th eigenfrequency of the system, and compare it with the experimental measurement. In this example, a ~ 21.3% difference is reported, which we assume is related to tip's flexibility. If the tip's flexibility effects were included in the LMTM, an additional decrease would have been expected in the eigenvalues. With the model used in this work to process experimental

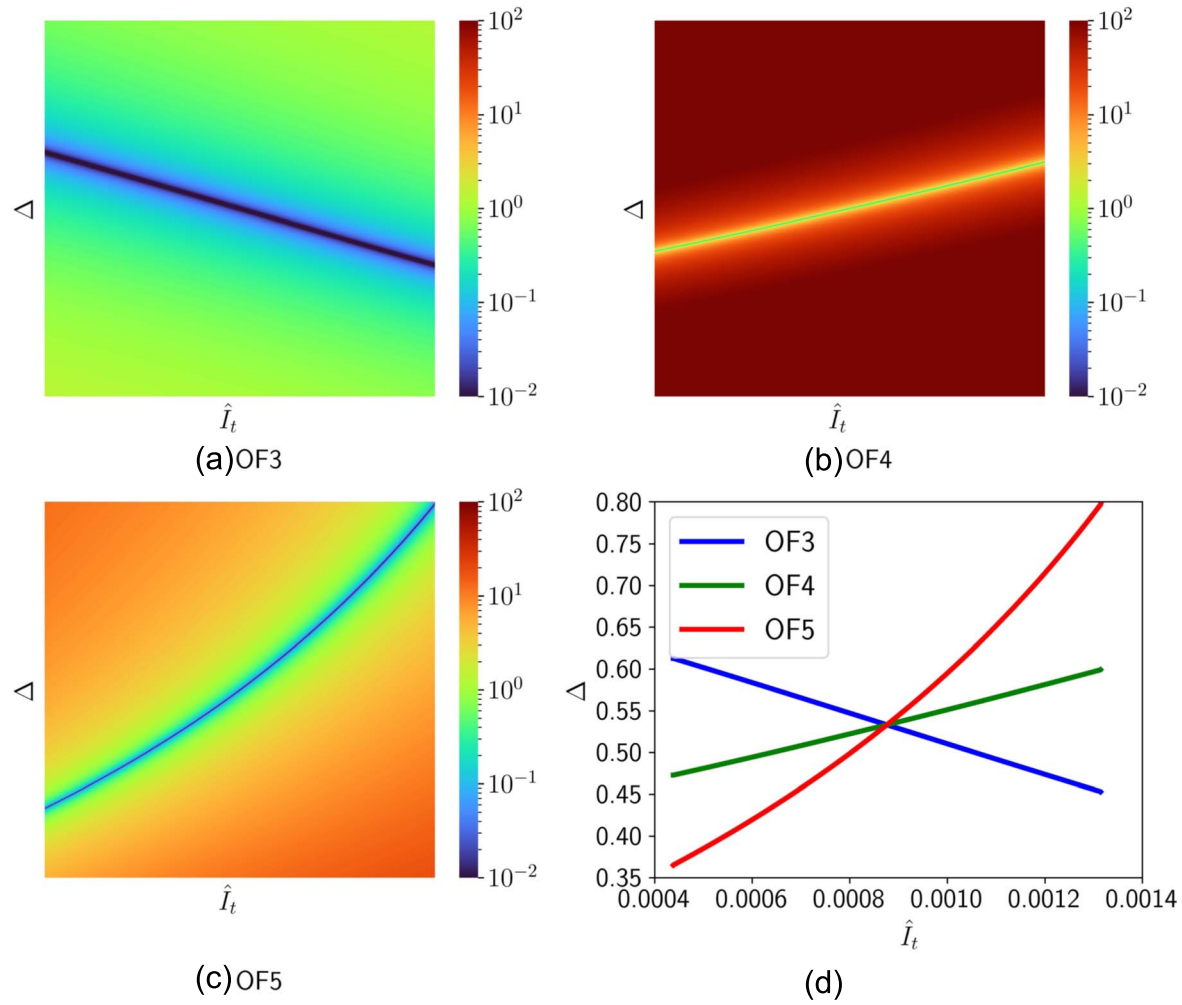

Figure 2. Heatmap graphical solution for 3 different types of objective functions error shown in (a), (b), and (c), and the crossing solution resulting from the minimum error curve shown in (d) for the modified sensor. The objective functions (OF) used are described in appendix.

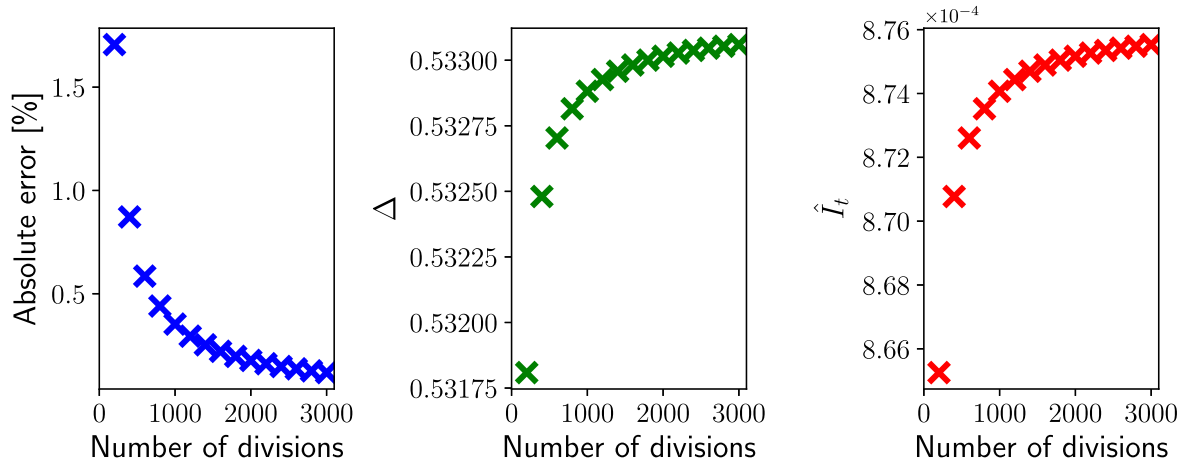

Figure 3. Convergence of the sum of absolute error of 12 different objective functions (see appendix) and their corresponding Δ and $\hat{I}_t$ values, obtained for the modified sensor.

eigenfrequencies (and neglecting tip flexibility), the model outputs increased Δ and $\hat{I}_t$ values, as can be seen in table 4, to compensate for the flexibility effects. A further discussion on the eigenvalues of different models is given in section 4.2.

The RMN sensor has a significantly large tip, with mass comparable to the mass of the sensor, as seen in table 4. Nonetheless, under the effect of gravity, the static deflection and the resulting curvature are negligible. In cases where

Table 3. Properties measured during AFM experimental setup and using SEM of the 25Pt300B RMN sensor.

Property	As measured	Remarks
L [μm]	300.5	Length of sensor
b [μm]	110.6	Width of sensor
h [μm]	5.5	Thickness of sensor
L_2 [μm]	113.0	Length of tip
f_1^0 [kHz]	11.8	Freely vibrating transverse 1st eigenfrequency
f_2^0 [kHz]	71.3	Freely vibrating transverse 2nd eigenfrequency
f_3^0 [kHz]	187.4	Freely vibrating transverse 3rd eigenfrequency
f_4^0 [kHz]	363.5	Freely vibrating transverse 4th eigenfrequency

large curvature is introduced, the vibration problem is altered significantly [35, 36].

2.5. Example problem 3: solution multiplicity

In this example we demonstrate how a certain set of 3 eigenfrequencies may lead to multiple solutions of the system parameters. We examine the Δ and $\hat{I}_t$ solution domain and use the resulting system parameters solutions to calculate the 4th eigenfrequency to distinguish between the solutions. Table 5 summarizes the input system parameters, the resulting first 4 eigenfrequencies, the additional solution which satisfies the system using the first 3 eigenfrequencies and its resulting 4th eigenfrequency denoted $\tilde{f}_4^0$. A graphical representation for the solutions multiplicity is given in figure 4(d).

Note that the multiple solutions share the same first 3 resonant frequencies, but they do not share the same eigenvalues or eigenmodes. Δ and $\hat{I}_t$ are nondimensional parameters and a specific set of them will lead to certain eigenvalues. $\tilde{C}$ is a dimensional parameter with units of time, relating the nondimensional eigenvalues to the dimensional eigenfrequencies.

The minimum curves in the heatmap representation of the 3 different objective functions given in figures 4(a)–(c) cross in two different solution points, as given in table 5 and shown in figure 4(d).

Once again, by increasing the number of divisions per a fixed range of Δ and $\hat{I}_t$, we minimize the error by better estimating the system parameters. In this example, where our domain includes two solutions, the Δ and $\hat{I}_t$ solutions corresponding to the minimum error, show a convergence to two different solutions, as seen in figure 5.

In order to distinguish between multiple solutions, we suggest the following steps:

1. Estimate Δ, $\hat{I}_t$, and $\tilde{C}$ based on the nominal dimensions, or SEM measurements, if available.
2. Use the 3-Mode approach with multiple initial conditions in a physically realistic range to solve for the system parameters. Suggested bounds: zero lower bound and approximately 4–5 times the nominal/estimated value for upper bound, depending on the expected accuracy of the dimensions.
3. If multiple solutions do not exist, use the resulting system parameters.
4. If multiple solutions do exist, use the resulting system parameters to calculate the predicted 4th eigenfrequency of the system from all the solutions found, and compare to the experimental 4th eigenfrequency. Use the solution with the minimal error from mode 4. If an experimental 4th eigenfrequency was not measured, use the solution with the minimal error from the nominal/estimated system parameters.

Table 4. System parameters as calculated using 3-Mode approach for the RMN sensor.

Source of data	$\hat{I}_t$	Δ	$\tilde{C}$[sec]
Estimated based on SEM measurements[a]	0.0060	0.3939	1.2583×10^{-4}
Three transverse modes (3-Mode approach)	0.0240	0.6868	1.4830×10^{-4}

[a] Also using $\rho_{Pt} = 21450\ \mathrm{kg/m^3}$ and $E_{Pt} = 171$ GPa.

3. Experimental validation

In this section we describe the AFM experiment performed for the validation of the new CR model introduced by Jaquez-Moreno *et al* [28]. System parameters were obtained in the example problems given in 2.3 and 2.4 for the modified sensor and the RMN sensor. Once the system parameters are known, standard CR methodology is used to calculate the sample's nondimensional stiffness. Additional CR spectroscopy is performed using the unmodified traditional sensor and all CR results are compared with additional nano-indentation sample measurements.

3.1. Experimental setup

CR spectroscopy is performed using an MFP-3D AFM (Asylum Research, Santa Barbara, CA). The CR spectra were acquired using three different setups. In the first setup, we use an unmodified sensor of type HQ-75-Au (Oxford Instruments) which is a standard silicon (Si) AFM probe (see figure 1(a)). In the second setup, we use the same HQ-75-Au sensor after modifying it by adding two glass spheres (see figure 1(b)). In the third setup, we use the RMN sensor descibed in section 2.4 (see figure 1(c)). The CR measurements are performed on two different synthetic glass samples, each placed on a transducer, hereinafter referred to as S_1 and S_2. In each of the discussed setups, multiple set point forces were applied, with the applied static deflections given in table 7. An example of the spectra measured on the two samples using the RMN sensor is provided in figure 6.

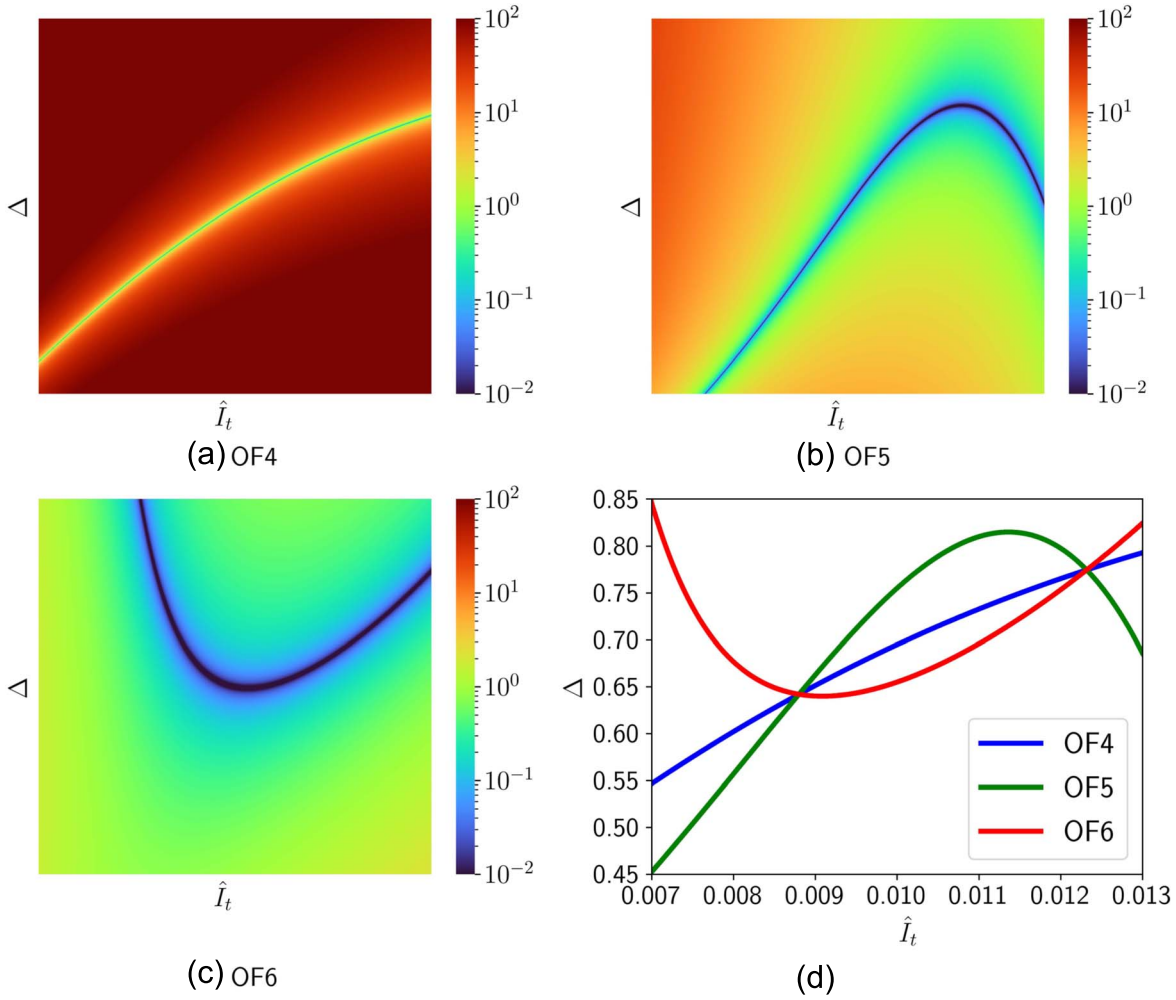

Figure 4. Heatmap graphical solution for 3 different types of objective functions error shown in (a), (b), and (c), and the multiple crossing solutions resulting from the minimum error curve shown in (d).

4. Results and discussion

4.1. Contact-resonance post processing

For the post processing of the CR spectra, obtained using the modified sensor and the RMN sensor, we first convert the experimental in-contact eigenfrequencies to the corresponding eigenvalues by using equation (3). In the next step, the characteristic equation, provided in equation (10) for reference, is used:

$$\begin{aligned}&[(-2\Delta\hat{I}_t(\beta L)^8+(2+(6\Delta\ell^2\phi\\&+6\hat{I}_t)\alpha)(\beta L)^4-18\ell^2\alpha^2\phi)\cos(\beta L)\\&+6(\beta L)\sin(\beta L)(-\hat{I}_t(\beta L)^6/3+\phi\ell^2\alpha(\beta L)^2\\&-\Delta(\beta L)^4/3+\alpha)]\cosh(\beta L)\\&+6(\beta L)(-\hat{I}_t(\beta L)^6/3+\phi\ell^2\alpha(\beta L)^2\\&+\Delta(\beta L)^4/3-\alpha)\sinh(\beta L)\cos(\beta L)+2\Delta\hat{I}_t(\beta L)^8\\&+(2+(-6\Delta\ell^2\phi-6\hat{I}_t)\alpha)(\beta L)^4+18\ell^2\alpha^2\phi=0.\end{aligned}\quad(10)$$

After finding the system parameters, Δ and $\hat{I}_t$, and the in-contact eigenvalues, the characteristic equation is a function of 3 more parameters: α the nondimensional sample stiffness, which is our primary interest and can be related to the sample's stiffness and indentation modulus by means of contact mechanics [39], $\ell=\frac{L_t}{L}$ the tip length to beam length ratio, and $\phi=\frac{k'}{k}$ the lateral sample stiffness and the normal sample stiffness ratio. Further investigation of the characteristic equation reveals that the latter two appear in the form $\ell^2\phi$ throughout the equation. Consequently, we solve for a combined constant $\ell^2\phi$. Since we have two unknown parameters, we require information from two different eigenfrequencies, measured at the same applied load. A graphical representation of the domain spanned by $\ell^2\phi$ and α will give a graphical curve crossing solution known as the 'mode-crossing' technique [40] (see figure 7(b)). For the unmodified sensor, we use the SSM for post processing using two in-contact eigenfrequencies for the determination of α the nondimensional sample stiffness, and $\gamma=\frac{L_1}{L}$ the nondimensional tip location. A 'mode-crossing' layout for the unmodified sensor is presented in figure 7(a).

Once we have obtained the nondimensional sample stiffness for each applied load on both samples for all 3 sensors, we may use the reference approach that allows us to relate the CR results to the ratio between the reduced modulus

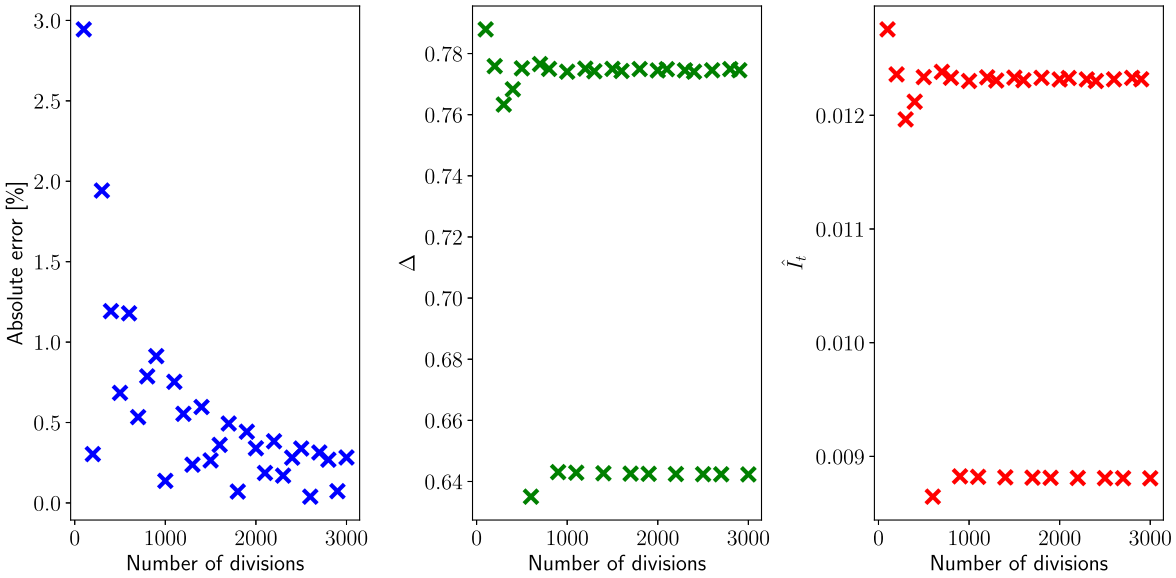

Figure 5. Convergence of the sum of absolute error of 12 different objective functions (see appendix) and their corresponding Δ and $\hat{I}_t$ values, obtained for the example problem solution multiplicity data. The solution for Δ and $\hat{I}_t$ converges to two separate solutions, prof of the solution multiplicity.

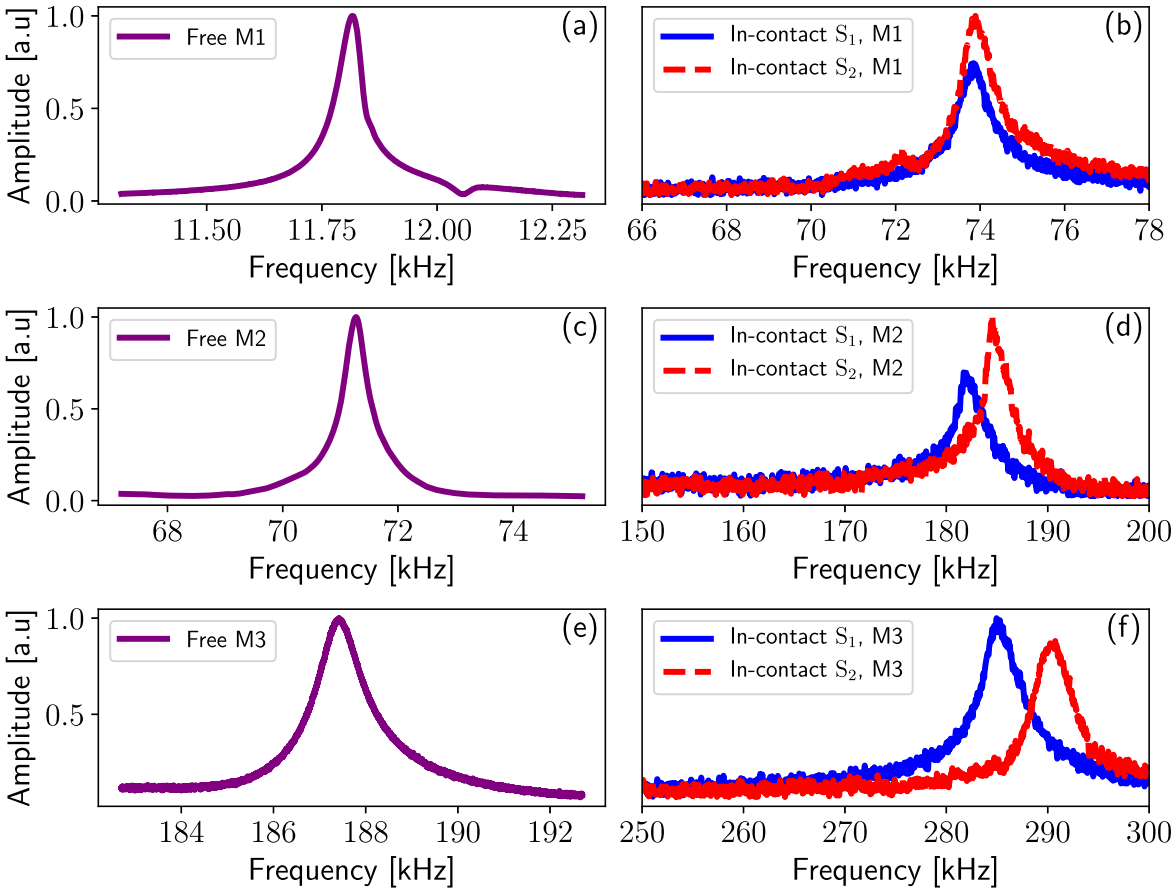

Figure 6. Examples of experimental data taken using the RMN sensor. (a), (c), and (e): spectra of the 1st, 2nd, and 3rd eigenfrequencies out of contact (free). (b), (d), (f): corresponding CR spectra (in-contact) for $d = 495.9$ [nm] on S_1 (solid blue line) and S_2 (dashed red line). M1, M2, and M3 are the 1st, 2nd, and 3rd eigenmodes correspondingly. Note that the CR eigenfrequencies shown in (b) for the 1st eigenmode are higher than the free 2nd eigenfrequency shown in (c). Furthermore, the 1st eigenfrequency CR spectrum does not capture the difference between the samples stiffness as this eigenmode reaches a nonsensitive region [37], unlike the 2nd and 3rd eigenmodes which show a clear difference between the samples. When an eigenmode reaches a nonsensitive region, measurements taken at different applied loads will lead to very similar values of the contact resonance frequency (f_n), leading to incorrect nondimensional sample stiffness (α) values and incorrect sample properties.

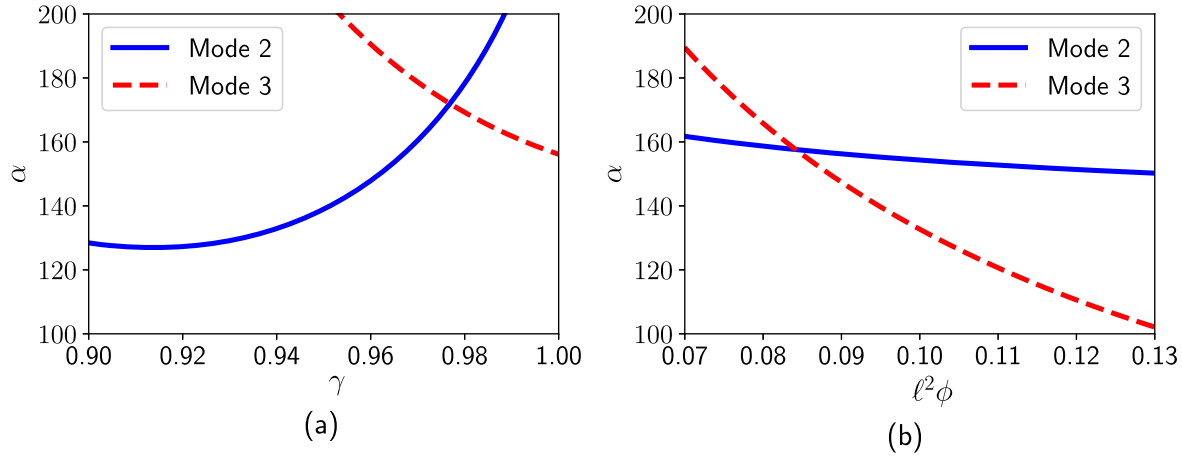

Figure 7. Nondimensional contact stiffness α as a function of γ for the unmodified sensor processed using the SSM in (a) and as a function of $\ell^2\phi$ for the RMN sensor processed using the LMTM in (b). Results are shown for the 2nd eigenfrequency (solid blue line) and the 3rd eigenfrequency (dashed red line) for both cases, with $f_2 = 1059.1$ [kHz] and $f_3 = 1838.1$ [kHz] for (a) and $f_2 = 184.8$ [kHz] and $f_3 = 290.4$ [kHz] for (b) (see table 7), both taken on S_2. For (b), recall that the α solution is a 2nd order polynomial, thus we have two possible solutions: the 2nd eigenfrequency is plotted using the positive square root solution of α and the 3rd eigenfrequency is plotted using the negative square root solution. The intersection point of the curves in each case, or the 'mode-crossing' location, indicates the solution values for α and γ, or α and $\ell^2\phi$.

Table 5. Example problem (solution multiplicity) eigenfrequencies calculated with system parameters: $\Delta = 0.642$, $\hat{I}_t = 0.0088$ and $\tilde{C} = 1.4 \times 10^{-4}$[sec] and equation (4) and equation (3). 2nd solution satisfying the first 3 eigenfrequencies: $\Delta = 0.7746$, $\hat{I}_t = 0.0123$ and $\tilde{C} = 1.3021 \times 10^{-4}$[sec]. Note that the two solutions share the same first 3 eigenfrequencies, but do not share the same eigenvalues, as $\tilde{C}$, the parameter relating the eigenvalues to the dimensional eigenfrequencies, is different for each solution. Therefore, the different solutions will not share the eigenmodes, but only the eigenfrequencies.

Property	As measured or calculated	Remarks
f_1^0 [kHz]	13.1	Freely vibrating transverse 1st eigenfrequency
f_2^0 [kHz]	97.6	Freely vibrating transverse 2nd eigenfrequency
f_3^0 [kHz]	236.6	Freely vibrating transverse 3rd eigenfrequency
f_4^0 [kHz]	485.6	Freely vibrating transverse 4th eigenfrequency
$\tilde{f}_4^0$ [kHz]	510.9	Freely vibrating transverse 4th eigenfrequency, calculated using the 2nd solution

of the two samples [41, 42]:

$$\frac{E^*_{S_1}}{E^*_{S_2}} = \left(\frac{\alpha_{S_1}}{\alpha_{S_2}}\right)^m, \tag{11}$$

where the reduced modulus E^* is a combination of the sample's and tip's indentation moduli such that $\frac{1}{E^*} = \frac{1}{M_{\text{sample}}} + \frac{1}{M_{\text{tip}}}$, and $m = 1$ and $m = 3/2$ represent a flat punch and spherical indenter respectively, as the two limiting cases [39]. In order to conclude our experimental work, we compare the data analysis using the LMTM and the SSM for the modified sensor and the RMN sensor, with the unmodified sensor analyzed using the SSM, along with nanoindentation data. The mean value of the α ratio $\left(\frac{\alpha_{S_1}}{\alpha_{S_2}}\right)$, for the 3 set point forces described in table 7, from each of the sensors/models discussed above, is plotted in figure 8 and summarizes our experimental validation. The data for the unmodified sensor analyzed using the SSM, as in common contact resonance practice, shows best results for a flat punch using 'mode-crossing' results from both eigenmodes pairs $n = 1,2$ (M12) and $n = 2,3$ (M23). The data for the modified sensor does not result in any value when analyzed using the SSM for M12, i.e. no 'mode-crossing' is found, nonetheless, fair results are obtained for the M23 data with a flat punch assumption. When analyzing the modified sensor using the LMTM, results align very well with the unmodified sensor analyzed using the SSM for both eigenmode pairs, assuming a flat punch (recall the modified sensor holds the same tip as the unmodified sensor, thus both performing well with the same tip shape is a good correlation). For the data collected using the RMN sensor, when analyzed using the SSM, no results are found. When analyzed using the LMTM, good results are obtained using the M23 and assuming a spherical indenter. Figure 6(b) shows the lack of sensitivity for the first eigenfrequency in contact, which can explain the M12 error. Furthermore, the flexibility of the RMN sensor tip can affect the estimation of the system parameters (see section 2.4), and the estimation of the sample stiffness for the sensitive M23 data, as the LMTM assumes a rigid tip. The expected value,

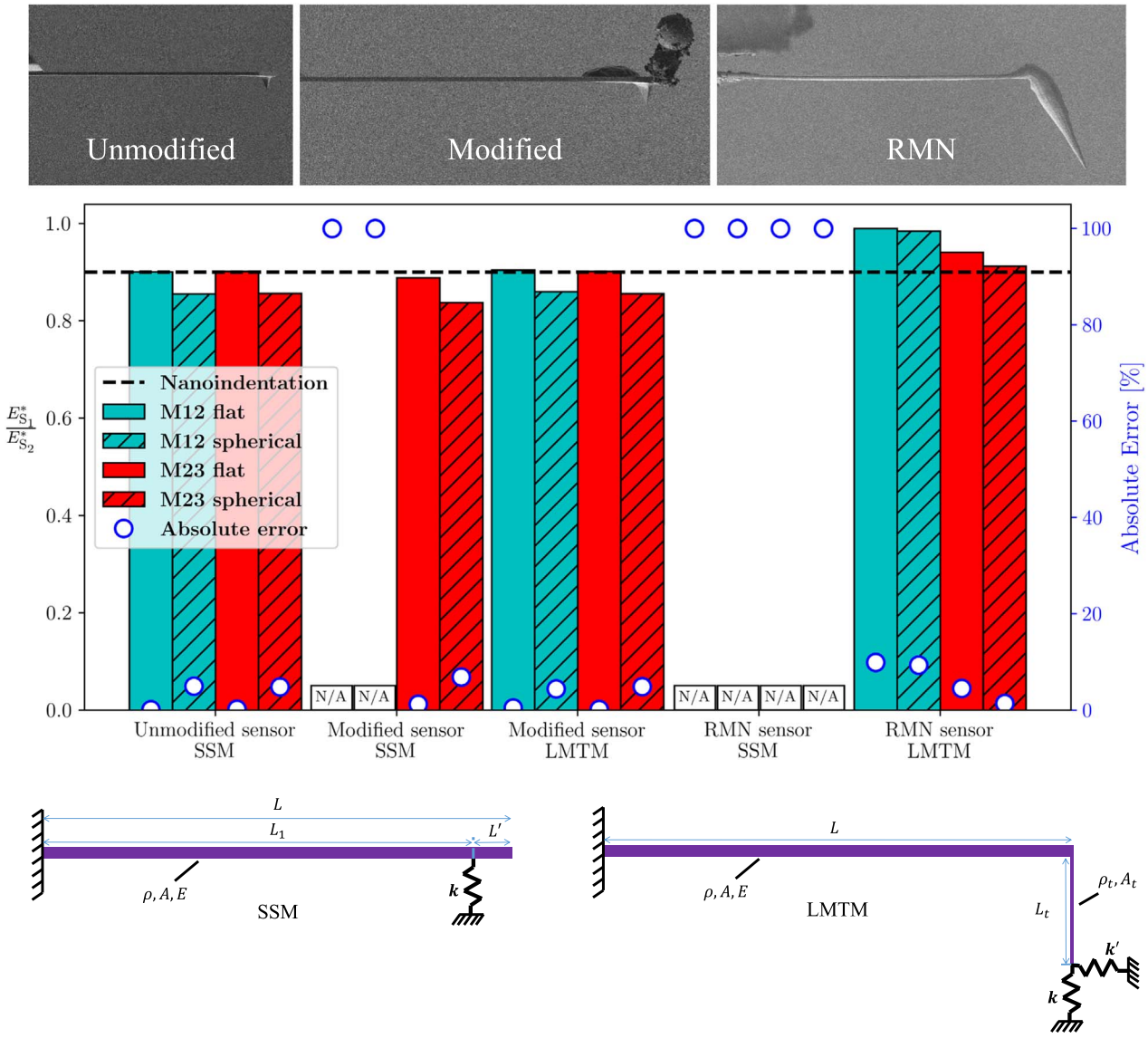

Figure 8. Experimental CR results analyzed using the SSM for all 3 sensors and also analyzed using the LMTM for the modified and RMN sensors. Each bar is the mean value of $\left(\frac{\alpha_{S1}}{\alpha_{S2}}\right)^m$ obtained from CR results with $m = 1$ for a flat punch and $m = 3/2$ for a spherical indenter, from all set point forces on both samples. The standard deviation for all cases presented here is smaller than 0.0064. Cases where no prediction was made by the SSM are denoted by 'N/A' and an absolute error of 100%.

plotted in black dashed line, represents the value $\frac{E^*_{S_1}}{E^*_{S_2}} = \frac{M_{S1}}{M_{S2}} \cdot \frac{M_{S2}+M_{tip}}{M_{S1}+M_{tip}} = 0.90$ obtained from the nanoindentation along with the tip's bulk indentation moduli as a benchmark (data provided in table 6). The difference in the $\frac{E^*_{S_1}}{E^*_{S_2}}$ values obtained for the silicon and platinum tips is smaller than 0.01. Other CR models that include an end mass, presented by: Rabe *et al* [2] and Muraoka [32], have not outperformed the results obtained by the LMTM, showing less than 5% error for the sensitive eigenmode pair $n = 2,3$ (M23).

In order to theoretically estimate the relative error of using the SSM for data that was obtained using long, massive tips, we consider the simple case of a colloidal probe. By varying the radius of the colloidal particle, we can simultaneously vary the tip length, the added tip mass, and the added tip rotational inertia. We use the LMTM, to produce CR frequencies for different colloidal particle radius, while also varying the sample stiffness. Then, we use the SSM along with the frequencies produced by the LMTM to

Table 6. Indentation modulus values for silicon and platinum tips and the two samples.

Property	Value	Remarks
M_{S_1} [GPa]	37.0 ± 0.8	Sample 1 indentation modulus
M_{S_2} [GPa]	42.0 ± 1.0	Sample 2 indentation modulus
M_{Si} [GPa]	165.0 [38]	Tip's indentation modulus, Si ⟨100⟩
M_{Pt} [GPa]	201.7 [28]	Tip's indentation modulus, Pt

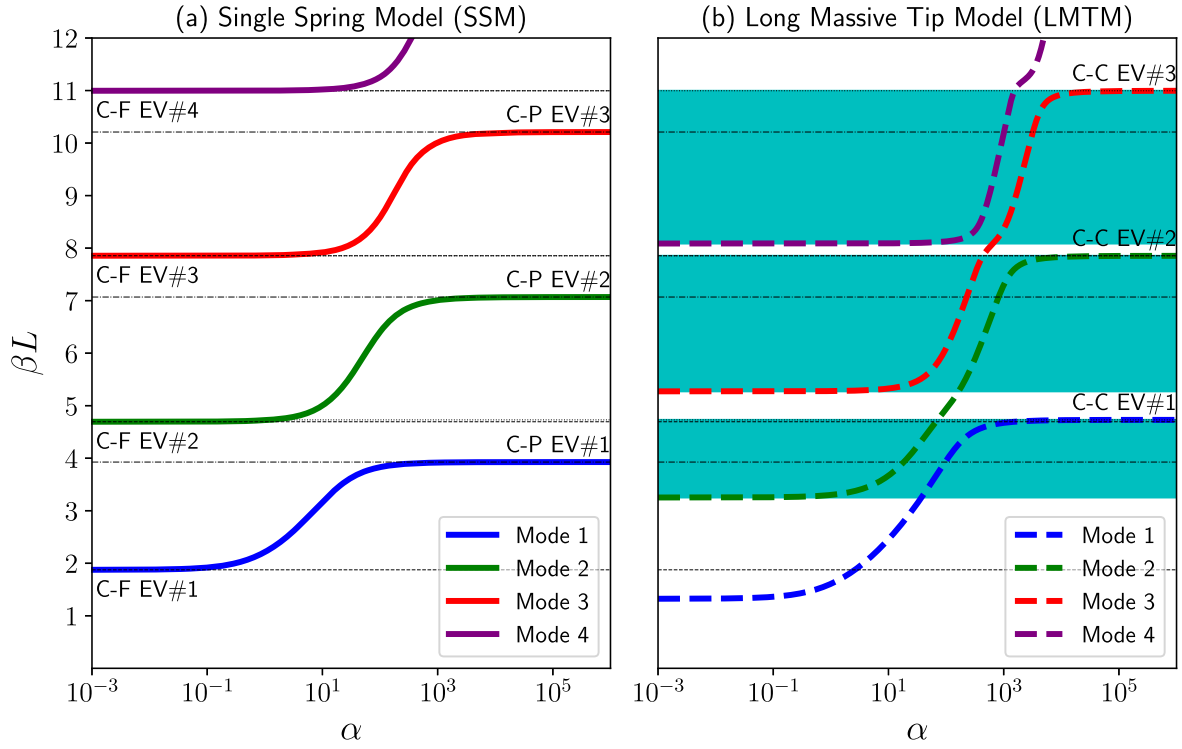

Figure 9. The first 4 eigenvalues (EV) as a function of the nondimensional sample stiffness α, using the SSM ((a) solid lines) and the LMTM ((b) dashed lines), with $\gamma = 1$ for the SSM, and $\Delta = 0.6868$, $\hat{I}_t = 0.0240$, and $\ell^2\phi = 0.0857$ for the LMTM. The EV boundaries are presented in (a) and (b) with horizontal black lines for the clamped-free first 4 EV (C-F EV: 1.8751, 4.6941, 7.8548, 10.9955) dashed line, the clamped-pinned first 3 EV (C-P EV: 3.9266, 7.0686, 10.2102) dash-dotted line, and the clamped-clamped first 3 EV (C-C EV: 4.7300, 7.8532, 10.9956) dotted line. In (b), light blue background color represents the range of eigenvalues resulting in a dual α solution.

predict the assigned sample stiffness using the mode crossing approach. We find that for $\Delta > 0.04$ the SSM will either not provide any solution (i.e. no 'mode-crossing'), or will result in large error. Note that in this work we use experimental cases where $\Delta \gg 0.04$.

4.2. Eigenvalue boundaries

In CR experiments, performed using a typical optical lever-based AFM system, the spectra are measured without specific knowledge of which eigenmode is contributing. The experimentalist would use upper and lower bounds of analytical eigenmodes to associate a resonance peak with the corresponding eigenmode. Traditionally, the lower and upper bounds are formed from the clamped-free and clamped-pinned boundary conditions for the E–B free response, and their corresponding eigenvalues. For the SSM, as the tip location (represented by the normal spring location along the beam) moves away from the beam end towards the clamped end, within the realistic tip location value of $0.9 < \gamma < 1$, the eigenvalue upper boundary increases but will not go higher than the clamped-clamped eigenvalue boundary. The clamped-clamped nth eigenvalue is approaching the $n+1$ clamped-free eigenvalue, with the increase in n. The inclusion of a lateral spring in the CR model will increase the clamped-clamped upper bound of the nth eigenvalue to a value higher than the clamped-free $n+1$ eigenvalue as was shown theoretically by Rabe [43]. The increase in the in-contact eigenvalue over the clamped-free eigenvalue of the following eigenmode, results in a unique phenomenon where an eigenfrequency, corresponding to an eigenvalue, may be associated with two different α values, as shown by Jaquez-Moreno *et al* [28]. This is also emphasized in the characteristic equation which can be brought into a form of a 2nd order polynomial in α (for CR models that include a lateral spring), thus having two positive real α solutions in some regions, each relating to a different eigenfrequency (see examples for CR models with lateral spring in [28, 39, 43]).

In order to distinguish between the two α solutions, a distinction between the the two eigenmodes is necessary. Considering the LMTM, we know that the effect from the lateral spring may increase the upper bound of the eigenvalues. With the inclusion of the added mass and rotational inertia of the tip, located at the beam end, we also have a decrease in the lower bound relating to the clamped-free boundary condition. This combination of reduced lower bound, due to the added mass, and increased upper bound, due to the lateral spring, paves the way for a case where the nth eigenfrequency in contact is at a higher frequency than the $n+1$ freely vibrating sensor. An experimental example of such a case is shown in figure 6 (b) and (c). This example of spectrum could be mistaken for a low α value corresponding to the 2nd eigenmode rather than a high α value corresponding to the 1st eigenmode. In order to avoid the

Table 7. CR experimental results performed with 3 different sensors, using the f_2 and f_3 flexural modes versus the cantilever static deflection, d. Also showing the values of the nondimensional tip location γ for the unmodified sensor, and $\ell^2\phi$ for the other two sensors, which should be constant values. The value of the nondimensional contact stiffness α, increases with the increase in the static deflection.

Unmodified sensor						Modified sensor						RMN sensor					
d [nm]	Sample	f_2[kHz]	f_3 [kHz]	γ	α	d [nm]	Sample	f_2 [kHz]	f_3 [kHz]	$\ell^2\phi$	α	d [nm]	Sample	f_2 [kHz]	f_3 [kHz]	$\ell^2\phi$	α
21.1	S_1	1039.1	1782.7	0.976	150.7	26.7	S_1	761.8	1269.1	0.000 689	186.7	297.6	S_1	179.6	282.7	0.0873	141.3
25.3	S_1	1039.3	1797.1	0.978	154.1	32.1	S_1	766.6	1270.3	0.000 718	189.4	396.7	S_1	181.2	284.3	0.0853	146.7
29.5	S_1	1041.2	1801.8	0.978	155.9	37.4	S_1	768.8	1271.1	0.000 744	190.6	495.9	S_1	181.9	285.1	0.0847	149.0
21.1	S_2	1056.1	1828.1	0.977	168.2	26.7	S_2	797.3	1275.0	0.000 752	207.2	297.6	S_2	182.7	287.0	0.0849	151.3
25.3	S_2	1058.1	1834.8	0.977	170.7	32.1	S_2	800.1	1275.6	0.000 762	208.9	396.7	S_2	184.0	288.4	0.0837	155.5
29.5	S_2	1059.1	1838.1	0.977	172.0	37.4	S_2	802.5	1276.1	0.000 769	210.3	495.9	S_2	184.8	290.4	0.0842	157.6

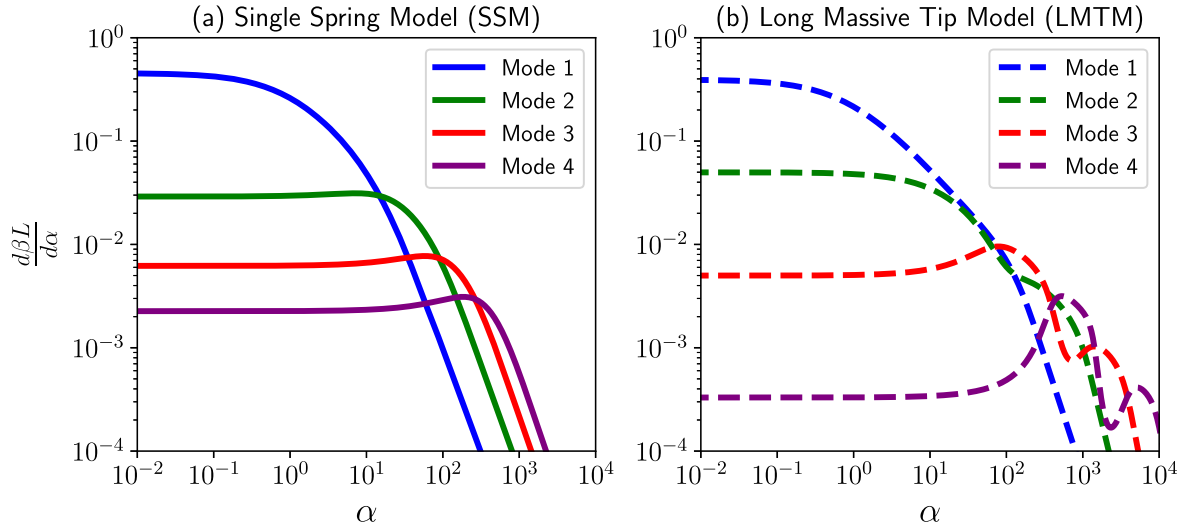

Figure 10. The sensitivity for the first 4 eigenvalues (EV) as a function of the nondimensional sample stiffness α, using the SSM ((a) solid lines) and the LMTM ((b) dashed lines), with $\gamma = 1$ for the SSM, and $\Delta = 0.6868$, $\hat{I}_t = 0.0240$, and $\ell^2\phi = 0.0857$ for the LMTM. In (b), the modal sensitivity does not decrease monotonically with α due to a secondary increase in the sensitivity.

aforementioned situation, we propose taking the following steps:

1. Use multiple set point forces during the CR experiment with both a minimal applied load and a high applied load (while minimizing sample and tip damage).
2. Use the LMTM and equation (3) to plot the eigenfrequencies as a function of α for the number of experimental eigenmodes found plus one using either an estimated $\ell^2\phi$ value, or using a mean value from the 'mode-crossings' performed. An example for such a plot is presented in figure 9.
3. Check for possible solution multiplicity if the $n+1$ free frequency is lower than the nth clamped-clamped frequency (as in figure 9(b) light blue regimes).
4. Identify CR experimental eigenfrequency within the frequency range described above.
5. Use the multiple set point loads applied to identify the shift in the CR eigenfrequencies, which should allow for a clear distinction between the different eigenmodes.

The eigenvalue sensitivity, $\frac{d\beta L}{d\alpha}$, is an important metric that can be related to the increase in CR frequency with an increase in the applied load. The SSM curve presented in figure 9(a), shows a smooth transition from the lower clamped-free bound to the upper clamped-pinned bound. In the LMTM curve presented in figure 9(b), we witness a relatively smooth transition for the first eigenmode, whereas for the higher eigenmodes, we witness a change in slope about halfway between the lower and upper bounds. These changes in slope correspond to changes in the CR sensitivity as presented in figure 10.

In common CR practice, 'mode-crossing' is traditionally performed using consecutive eigenmodes, i.e. $n = 1,2$, $n = 2,3$ and so forth, to estimate the nondimensional sample stiffness and another system parameter, based on two in-contact eigenmodes. Using the two eigenmodes with maximum sensitivity, will result in optimal CR accuracy [39]. The CR sensitivity obtained using the LMTM shows multiple maxima for the 3rd and 4th eigenmode curves. The multiple maxima are spaced by approximately a decade, and the maximum value of the 2nd maximum is lower by a decade. Nevertheless, this phenomenon still contributes to an overall increase in the sensor's performance as it extends the sensitivity range of the contributing eigenmodes. Along with the multiple maxima observed and the extended sensitivity range, we also witness a range where maximum sensitivity for two eigenmodes is not necessarily achieved with consecutive eigenmodes. In figure 10(b) at $400 < \alpha < 1000$, eigenmodes $n = 2$ and $n = 4$ exhibit higher sensitivity than eigenmode $n = 3$. With this finding, we propose using mode pairs with maximum sensitivity for improved CR accuracy, which are not necessarily consecutive modes. The reason for the multiple maxima comes from the normal and lateral springs representing the sample's stiffness. When the normal deflection of the beam reduces to nearly zero due to the increasing normal spring force, i.e. the normal motion experiences a 'pinned' condition, the lateral spring still allows the beam's end to rotate, providing the system additional sensitivity to measure the sample's stiffness. The beam's slope at the distal end increases with increasing mode number, contributing to the increasing sensitivity seen at higher non-dimensional stiffness due to the lateral spring [39, 43]. This increase in sensitivity with mode number at higher non-dimensional stiffness is seen in figure 10(b).

5. Conclusions

We have experimentally validated a CR model that incorporates effects from tip length, mass, and rotational inertia. In order to effectively use the aforementioned model,

a new technique was developed and demonstrated for the determination of system parameters via a solution to a system of nonlinear equations. The solution relies solely on the sensor's free vibrating transverse eigenfrequencies, as in traditional CR practice, with no *a priori* knowledge of the sensor's dimensions or of the un-tipped system. Furthermore, we have developed a graphical representation of the solution domain allowing users to analyze solution multiplicity. The graphical representation is based on minimization of objective functions comprised from the E–B beam solution dispersion relation, solely using data from 3 free eigenfrequencies. The use of long, massive tips not only affects the free eigenfrequencies but also the in-contact spectra. The use of traditional upper and lower bounds of the system's eigenvalues are invalid, and experimental spectra from the 1st eigenfrequency in-contact is demonstrated to be higher than the free 2nd eigenfrequency. This work opens new opportunities for the use of advanced sensors, commercially available for AFM, in contact resonance mode. Such work may include colloidal sensors probing a sensitive biological sample, a sensor equipped with a long needle tip probing a sample in liquid environment while the sensor's body remains out of the liquid (Trolling mode), or the use of Quartz tuning fork which obviates the use of a laser system for the sensing of the beam deflections and has piconewton force resolution. We have examined the possible error of using a simpler model such as the SSM in analyzing data from sensors with large, massive tips, and conclude that a $\Delta > 0.04$ requires the use of the LMTM. Experimental CR results for the RMN sensor analyzed using the LMTM, showed an absolute error of 1.4%–4.5% relative to the nanoindentation experiments, where the SSM failed to produce any solution.

In the future, we aim to extend the CR model validated here, that assumes a rigid tip, to include effects from the tip's elasticity which will affect both the out-of-contact case along with the in-contact. Past CR models were developed to include effects from different system parameters for increased accuracy of the sample's stiffness, but have failed to become common practice due to uncertainty in the multiple system parameters, as discussed in section 2. We will continue to research practical techniques that will allow the use of a CR model that includes multiple system parameters. Future work on the multiplicity of solutions found by the minimization technique developed here is needed for the determination of the correct solution. Furthermore, the determination of the most effective objective function may be further investigated and is not discussed here.

Acknowledgments

This material is based in part upon work supported by the National Science Foundation under Grant No. 1934772.

Data availability statement

All data that support the findings of this study are included within the article (and any supplementary files).

Appendix

Here we present the objective functions (OF) used to calculate the system parameters error in section 2.3 and section 2.5:

1. $\mathrm{OF1} = \frac{\beta_2 L - \beta_3 L}{\beta_1 L} - \frac{\sqrt{f_2^0} - \sqrt{f_3^0}}{\sqrt{f_1^0}}$
2. $\mathrm{OF2} = \frac{\beta_1 L - \beta_3 L}{\beta_2 L} - \frac{\sqrt{f_1^0} - \sqrt{f_3^0}}{\sqrt{f_2^0}}$
3. $\mathrm{OF3} = \frac{\beta_1 L - \beta_2 L}{\beta_3 L} - \frac{\sqrt{f_1^0} - \sqrt{f_2^0}}{\sqrt{f_3^0}}$
4. $\mathrm{OF4} = \frac{(\beta_2 L)^2 - (\beta_3 L)^2}{(\beta_1 L)^2} - \frac{f_2^0 - f_3^0}{f_1^0}$
5. $\mathrm{OF5} = \frac{(\beta_1 L)^2 - (\beta_3 L)^2}{(\beta_2 L)^2} - \frac{f_1^0 - f_3^0}{f_2^0}$
6. $\mathrm{OF6} = \frac{(\beta_1 L)^2 - (\beta_2 L)^2}{(\beta_3 L)^2} - \frac{f_1^0 - f_2^0}{f_3^0}$
7. $\mathrm{OF7} = \frac{(\beta_2 L)^4 - (\beta_3 L)^4}{(\beta_1 L)^4} - \frac{(f_2^0)^2 - (f_3^0)^2}{(f_1^0)^2}$
8. $\mathrm{OF8} = \frac{(\beta_1 L)^4 - (\beta_3 L)^4}{(\beta_2 L)^4} - \frac{(f_1^0)^2 - (f_3^0)^2}{(f_2^0)^2}$
9. $\mathrm{OF9} = \frac{(\beta_1 L)^4 - (\beta_2 L)^4}{(\beta_3 L)^4} - \frac{(f_1^0)^2 - (f_2^0)^2}{(f_3^0)^2}$
10. $\mathrm{OF10} = \frac{(\beta_1 L)^2}{f_1^0} + \frac{(\beta_2 L)^2}{f_2^0} - 2\frac{(\beta_3 L)^2}{f_3^0}$
11. $\mathrm{OF11} = \frac{(\beta_2 L)^2}{f_2^0} + \frac{(\beta_3 L)^2}{f_3^0} - 2\frac{(\beta_1 L)^2}{f_1^0}$
12. $\mathrm{OF12} = \frac{(\beta_1 L)^2}{f_1^0} + \frac{(\beta_3 L)^2}{f_3^0} - 2\frac{(\beta_2 L)^2}{f_2^0}.$

ORCID iDs

Nadav Zimron-Politi https://orcid.org/0000-0001-6141-3560
Ryan C Tung https://orcid.org/0000-0003-2862-6980

References

[1] Rabe U and Arnold W 1994 Acoustic microscopy by atomic force microscopy *Appl. Phys. Lett.* **64** 1493–5
[2] Rabe U, Janser K and Arnold W 1996 Vibrations of free and surface-coupled atomic force microscope cantilevers: theory and experiment *Rev. Sci. Instrum.* **67** 3281–93
[3] Ding X, Kuang B, Xiong C, Mao R, Xu Y, Wang Z and Hu H 2022 A super high aspect ratio atomic force microscopy probe for accurate topography and surface tension measurement *Sensors Actuators* A **347** 113891
[4] Efremov Y M, Suter D M, Timashev P S and Raman A 2022 3d nanomechanical mapping of subcellular and sub-nuclear structures of living cells by multi-harmonic afm with long-tip microcantilevers *Sci. Rep.* **12** 529
[5] Jafari A and Sadeghi A 2023 A new insight into the mechanical properties of nanobiofibers and vibrational

behavior of atomic force microscope beam considering them as the samples *J. Mech. Behav. Biomed. Mater.* **142** 105842
[6] Sajjadi M, Chahari M, Pishkenari H N and Vossoughi G 2022 Designing nonlinear observer for topography estimation in trolling mode atomic force microscopy *J. Vib. Control* **28** 3890–905
[7] Guan D, Charlaix E, Qi R Z and Tong P 2017 Noncontact viscoelastic imaging of living cells using a long-needle atomic force microscope with dual-frequency modulation *Phys. Rev. Appl.* **8** 044010
[8] Minary-Jolandan M, Tajik A, Wang N and Yu M F 2012 Intrinsically high-q dynamic afm imaging in liquid with a significantly extended needle tip *Nanotechnology* **23** 235704
[9] Mohammadi S Z, Moghadam M and Pishkenari H N 2019 Dynamical modeling of manipulation process in trolling-mode afm *Ultramicroscopy* **197** 83–94
[10] Shibata M, Uchihashi T, Ando T and Yasuda R 2015 Long-tip high-speed atomic force microscopy for nanometer-scale imaging in live cells *Sci. Rep.* **5** 8724
[11] Yamada Y, Ichii T, Utsunomiya T, Kimura K, Kobayashi K, Yamada H and Sugimura H 2023 Fundamental and higher eigenmodes of qplus sensors with a long probe for vertical-lateral bimodal atomic force microscopy *Nanoscale Adv.* **5** 840–50
[12] Martin-Jimenez D, Ruppert M G, Ihle A, Ahles S, Wegner H A, Schirmeisen A and Ebeling D 2022 Chemical bond imaging using torsional and flexural higher eigenmodes of qplus sensors *Nanoscale* **14** 5329–39
[13] Ruppert M G, Martin-Jimenez D, Yong Y K, Ihle A, Schirmeisen A, Fleming A J and Ebeling D 2022 Experimental analysis of tip vibrations at higher eigenmodes of qplus sensors for atomic force microscopy *Nanotechnology* **33** 185503
[14] Giessibl F J 2019 The qplus sensor, a powerful core for the atomic force microscope *Rev. Sci. Instrum.* **90** 011101
[15] Pürckhauer K, Weymouth A J, Pfeffer K, Kullmann L, Mulvihill E, Krahn M P, Müller D J and Giessibl F J 2018 Imaging in biologically-relevant environments with afm using stiff qplus sensors *Sci. Rep.* **8** 9330
[16] Yamada Y, Ichii T, Utsunomiya T and Sugimura H 2019 Simultaneous detection of vertical and lateral forces by bimodal afm utilizing a quartz tuning fork sensor with a long tip *Jpn. J. Appl. Phys.* **58** 095003
[17] Cihan E, Heier J, Lubig K, Graf S, Muller F A and Gnecco E 2023 Dynamics of sliding friction between laser-induced periodic surface structures (lipss) on stainless steel and pmma microspheres *ACS Appl. Mater. Interfaces* **15** 14970–8
[18] Li X, van der Gucht J, Erni P and de Vries R 2023 Active microrheology of protein condensates using colloidal probe-afm *J. Colloid Interface Sci.* **632** 357–66
[19] Chighizola M, Puricelli L, Bellon L and Podestà A 2021 Large colloidal probes for atomic force microscopy: Fabrication and calibration issues *J. Mol. Recognit.* **34** e2879
[20] Eskhan A and Johnson D 2022 Microscale characterization of abiotic surfaces and prediction of their biofouling/anti-biofouling potential using the afm colloidal probe technique *Adv. Colloid Interface Sci.* **310** 102796
[21] Kappl M and Butt H J 2002 The colloidal probe technique and its application to adhesion force measurements *Part. Part. Syst. Charact.: Meas. Description Part. Prop. Behav. Powders Other Disperse Syst.* **19** 129–43
[22] Francius G, Hemmerlé J, Ohayon J, Schaaf P, Voegel J C, Picart C and Senger B 2006 Effect of crosslinking on the elasticity of polyelectrolyte multilayer films measured by colloidal probe afm *Microsc. Res. Tech.* **69** 84–92
[23] Nguyen Q D, Oh E S and Chung K H 2019 Nanomechanical properties of polymer binders for li-ion batteries probed with colloidal probe atomic force microscopy *Polym. Test.* **76** 245–53
[24] Parvini C H, Cartagena-Rivera A X and Solares S D 2022 Viscoelastic parameterization of human skin cells characterize material behavior at multiple timescales *Commun. Biol.* **5** 17
[25] Solares S D and Cartagena-Rivera A X 2022 Frequency-dependent nanomechanical profiling for medical diagnosis *Beilstein J. Nanotechnol.* **13** 1483–9
[26] Stylianou A, Kontomaris S V, Grant C and Alexandratou E 2019 Atomic force microscopy on biological materials related to pathological conditions *Scanning* **2019** 8452851
[27] Lyonnais S, Hénaut M, Neyret A, Merida P, Cazevieille C, Gros N, Chable-Bessia C and Muriaux D 2021 Atomic force microscopy analysis of native infectious and inactivated sars-cov-2 virions *Sci. Rep.* **11** 11885
[28] Jaquez-Moreno T, Aureli M and Tung R C 2019 Contact resonance atomic force microscopy using long, massive tips *Sensors* **19** 4990
[29] Yuya P, Hurley D and Turner J A 2008 Contact-resonance atomic force microscopy for viscoelasticity *J. Appl. Phys.* **104** 074916
[30] Rabe U, Turner J and Arnold W 1998 Analysis of the high-frequency response of atomic force microscope cantilevers *Appl. Phys.* A **66** S277–82
[31] Meirovitch L 1967 *Analytical Methods in Vibrations* (New York, NY: MacMillan)
[32] Muraoka M 2002 Sensitive detection of local elasticity by oscillating an afm cantilever with its mass concentrated *JSME Int. J.* A **45** 567–72
[33] Rabe U, Hirsekorn S, Reinstädtler M, Sulzbach T, Lehrer C and Arnold W 2006 Influence of the cantilever holder on the vibrations of afm cantilevers *Nanotechnology* **18** 044008
[34] Hurley D C and Turner J A 2007 Measurement of poisson's ratio with contact-resonance atomic force microscopy *J. Appl. Phys.* **102** 033509
[35] Chidamparam P and Leissa A W 1993 Vibrations of planar curved beams, rings, and arches *ASME. Appl. Mech. Rev.* **46** 467–83
[36] Chang C S and Hodges D 2009 Vibration characteristics of curved beams *J. Mech. Mater. Struct.* **4** 675–92
[37] Turner J A and Wiehn J S 2001 Sensitivity of flexural and torsional vibration modes of atomic force microscope cantilevers to surface stiffness variations *Nanotechnology* **12** 322
[38] Rabe U, Amelio S, Kopycinska M, Hirsekorn S, Kempf M, Goken M and Arnold W 2002 Imaging and measurement of local mechanical material properties by atomic force acoustic microscopy *Surf. Interface Anal.* **33** 65–70
[39] Hurley D C 2009 Contact resonance force microscopy techniques for nanomechanical measurements *Applied Scanning Probe Methods XI* (Berlin: Springer) pp 97–138
[40] Rabe U, Amelio S, Kester E, Scherer V, Hirsekorn S and Arnold W 2000 Quantitative determination of contact stiffness using atomic force acoustic microscopy *Ultrasonics* **38** 430–7
[41] Rabe U, Amelio S, Kopycinska M, Hirsekorn S, Kempf M, Göken M and Arnold W 2002 Imaging and measurement of local mechanical material properties by atomic force acoustic microscopy *Surf. Interface Anal.* **33** 65–70
[42] Hurley D C, Shen K, Jennett N and Turner J A 2003 Atomic force acoustic microscopy methods to determine thin-film elastic properties *J. Appl. Phys.* **94** 2347–54
[43] Rabe U 2006 Atomic force acoustic microscopy *Applied Scanning Probe Methods II* (Berlin: Springer) pp 37–90